J Mater Sci

Chemical routes to materials

Synthesis and characterization of zirconium oxide-based catalysts for the oxygen reduction reaction via the heat treatment of zirconium polyacrylate in an ammonia atmosphere

Atsuhiro Ueno[1], Satoshi Seino[1,*], Yushi Tamaki[1], Yuta Uetake[1,2], Takaaki Nagai[3], Ryuji Monden[3], Akimitsu Ishihara[3], and Takashi Nakagawa[1]

[1] *Graduate School of Engineering, Osaka University, 2-1 Yamadaoka, Suita, Osaka 565-0871, Japan*
[2] *Innovative Catalysis Science Division, Institute for Open and Transdisciplinary Research Initiatives (ICS-OTRI), Osaka University, 2-1 Yamadaoka, Suita, Osaka 565-0871, Japan*
[3] *Institute of Advanced Sciences, Yokohama National University, 79-5 Tokiwadai, Hodogaya-Ku, Yokohama 240-8501, Japan*

Received: 7 November 2024
Accepted: 7 January 2025

ABSTRACT

Zirconium oxide-based catalysts for the oxygen reduction reaction (ORR) in polymer electrolyte fuel cells were synthesized via heat treatment of zirconium polyacrylate in an NH_3 atmosphere. The effects of gas atmosphere and heat treatment temperature on the material structure were systematically examined. The formation of zirconium oxide nanoparticles and carbon residues, which act as electron conduction paths, was observed in all samples. The structure of the material varied significantly depending on the heat treatment conditions. The samples heat-treated in the NH_3 atmosphere showed greater exposure to zirconium oxide nanoparticles and an increase in the specific surface area of the carbon residue caused by NH_3-induced etching. In addition, the conductivity of the carbon residue increased, and its quantity decreased with increasing heat treatment temperature. This trade-off was optimally controlled at 800 °C, which resulted in a high rest potential and a large ORR current density. This study demonstrates that the heat treatment of organometallic complexes in an NH_3 atmosphere is highly effective for exposing metal oxide nanoparticles and increasing the specific surface area of the carbon residue, providing valuable insights into the design of electron conduction paths for metal oxide-based catalysts.

Handling Editor: Pedro Camargo.

Address correspondence to E-mail: seino@mit.eng.osaka-u.ac.jp

https://doi.org/10.1007/s10853-025-10620-3
Published online: 21 January 2025

GRAPHICAL ABSTRACT

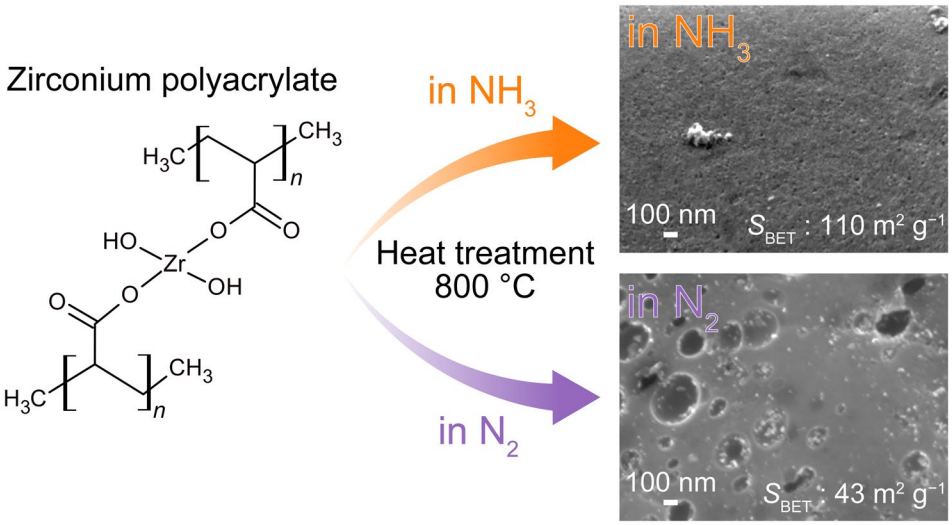

Introduction

Polymer electrolyte fuel cells (PEFCs) have attracted considerable attention as next-generation power sources for vehicles and households owing to their high energy conversion efficiency and the absence of greenhouse gas emissions during power generation. However, the widespread commercialization of PEFCs is limited by using platinum catalysts in the cathodes because platinum is a rare and expensive resource. Various non-platinum cathode catalysts have been developed to address this issue [1, 2]. Among these, Fe/N/C catalysts have attracted attention as highly efficient catalysts with high oxygen reduction reaction (ORR) activity; however, their durability in acidic media remains insufficient [3]. Other non-platinum cathode catalysts include Group IV and V metal oxide-based catalysts such as titanium, zirconium, niobium, and tantalum [4–9]. These catalysts are considered promising in terms of durability, owing to their high chemical stability in acidic media. However, metal oxide-based catalysts have low electrical conductivity, which hinders electron conduction to the active sites and reduces the ORR current density. Thus, it is necessary to form an electron conduction path that connects the current collector to the active sites on the oxide surface.

One approach to forming an electron conduction path is to support oxide nanoparticles on conductive supports, such as carbon black or carbon nanotubes. This method enables the formation of a macro-electron conduction path that connects the current collector to the oxide nanoparticles. However, relying solely on a macro-conduction path may not ensure efficient electron conduction to the active sites on the oxide surface and could limit the ORR. Therefore, the formation of a local micro-electron conduction path that connects the oxide nanoparticles to the active sites is necessary, in addition to the macro-conduction path. We previously reported that the carbon residue deposited during the heat treatment of oxy-zirconium phthalocyanine and multiwalled carbon nanotubes in an Ar atmosphere containing 2% H_2 and 0.05% O_2 acted as a micro-electron conduction path, promoting the ORR [10]. Furthermore, we reported an enhancement in the ORR activity of niobium oxide nanoparticle catalysts by forming a carbon residue, which creates a micro-conduction path through the decomposition of polyacrylonitrile included in the metal precursor [11]. In addition, Takeuchi et al. reported that a zirconium oxide-based catalyst synthesized by heat-treating Fe-added pyrazinecarboxylate zirconium in an Ar atmosphere containing 2% H_2 and 0.05% O_2 showed an excellent ORR onset potential of 0.917 V vs. reversible hydrogen electrode (RHE) in a 0.5 mol dm^{-3} H_2SO_4 solution [12]. In this catalyst, the carbon residue derived from pyrazinecarboxylate acts as an electron conduction path, functioning without a carbon support and connecting the current collector to the active sites on the oxide surface. This approach

not only enables the formation of an efficient electron conduction path, but also increases the content of oxides with active sites, enhancing the ORR mass activity. Therefore, the approach of depositing carbon residues derived from ligands via the heat treatment of organometallic complexes to form an electron conduction path connecting the current collector to the active sites on the oxide surface is considered highly promising. However, it is necessary to properly control the amount of carbon residue when it is used as an electron conduction path. An electron conduction path may be formed when the amount of carbon residue is large. However, the active sites on the oxide surface may be covered, thereby hindering the mass transfer of oxygen molecules and potentially limiting the ORR. By contrast, the active sites on the oxide surface may be exposed if the amount of carbon residue is small. However, the formation of an electron conduction path may be insufficient, thus limiting the ORR. Therefore, it is necessary to develop a synthetic method that enables the properly controlled formation of electron conduction paths.

Recently, our research group synthesized titanium oxynitride catalysts via heat treatment of titanium-based organometallic complexes in an NH_3 atmosphere [13]. This method enabled the formation of active sites by nitrogen doping of titanium oxide using NH_3 and the formation of an electron conduction path via the deposition of carbon residue derived from the ligands. Heat treatment in an NH_3 atmosphere not only serves as a process for nitrogen doping into titanium oxide, but also enables control over the amount of carbon residue. In this study, zirconium was selected as the target element, and zirconium oxide-based catalysts were synthesized via heat treatment of zirconium-based organometallic complexes in an NH_3 atmosphere. A schematic representation of this process is shown in Fig. 1. In this study, heat treatment in an NH_3 atmosphere was considered as the process for forming an electron conduction path to control the amount of carbon residue, conductivity, and morphology to form an electron conduction path suitable for the ORR.

Materials and methods

Preparation of catalyst precursor

Zirconium butoxide (ca. 80% in 1-butanol, 1.4 cm^3, 4 mmol, Tokyo Chemical Industry Co., Ltd.), acetylacetone (3.6 cm^3, Fujifilm Wako Pure Chemical Corp.), and acetic acid (4.3 cm^3, Fujifilm Wako Pure Chemical Corp.) were combined to prepare a zirconium acetylacetonate acetate solution. In addition, 10% aqueous solution of polyacrylic acid (average molecular weight: 25,000) (20 g, 28 mmol, Fujifilm Wako Pure Chemical Corp.), ethanol (40 cm^3, Fujifilm Wako Pure Chemical Corp.), acetic acid (20 cm^3, Fujifilm Wako Pure Chemical Corp.), 5 wt.% Nafion® dispersion (0.2 cm^3, 0.04 mmol, DE520 CS type, Fujifilm Wako Pure Chemical Corp.), and iron acetate (68 mg, 0.4 mmol, Tokyo Chemical Industry Co., Ltd.) were combined and the solution was stirred for 6 h at room temperature using a magnetic stirrer. Subsequently, a zirconium acetylacetonate acetate solution was added to the mixture and stirred overnight at the same temperature. The mixture was then homogenized for 30 min. Finally, the solvent was evaporated at 60 °C using a rotary evaporator to obtain zirconium polyacrylate (ZrPAA) powder.

Synthesis of catalysts

The ZrPAA powder (1 g) was accurately weighed and placed in a quartz glass inner case (Motoyama Co.,

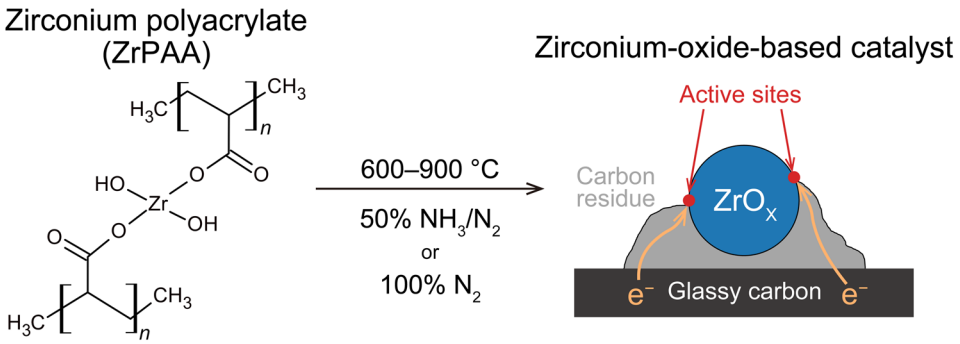

Figure 1 Schematic diagram of the synthesis of the zirconium oxide-based catalyst via the heat treatment of zirconium polyacrylate.

Ltd.), which was subsequently inserted into the furnace tube of a rotary kiln furnace (RK-0330, Motoyama Co., Ltd.). An atmosphere of either 50% NH_3/N_2 gas or 100% N_2 gas was introduced at the flow rate of 350 cm^3 min^{-1}, and the temperature was increased from room temperature to the target temperature (600, 700, 800, or 900 °C) throughout 1 h. After maintaining the temperature for 1 h, 100% N_2 gas was introduced for cooling to room temperature. After cooling, the samples were ground in an agate mortar for 15 min to obtain catalyst powder. The obtained catalyst powders were denoted as 800°C_N_2, 600°C_NH_3, 700°C_NH_3, 800°C_NH_3, and 900°C_NH_3.

Characterization

The crystal structure of the synthesized catalyst was characterized using powder X-ray diffraction (XRD; MiniFlex 600, Rigaku Corp.) with Cu-Kα radiation operated at 40 kV and 15 mA. Measurements were conducted over a 2θ range of 20–70° using a non-reflective silicon sample holder. The crystallite size was calculated from the diffraction peaks corresponding to monoclinic ZrO_2 (m-ZrO_2) in the $(1\bar{1}1)$ plane and tetragonal ZrO_2 (t-ZrO_2) in the (101) plane using Scherrer equation as shown in Eq. (1):

$$d = \frac{0.9\lambda}{\beta\cos\theta} \tag{1}$$

where d, λ, β, and θ represent the crystallite size, X-ray wavelength, full width at half maximum of the diffraction peak, and diffraction angle, respectively. The chemical states of the catalyst nanoparticles were evaluated using Zr K-edge X-ray absorption spectroscopy (XAS) measurements. The XAS measurements were performed at the NW10A beamline of KEK using the transmission method. The chemical composition ratio of the catalysts was estimated by linear combination fitting (LCF) analysis using the reference spectra of m-ZrO_2 and t-ZrO_2. The detailed measurement procedure is described in the Supporting Information (S2. X-ray absorption spectroscopy). Morphological observations and elemental analyses of the catalysts were performed using a transmission electron microscope (TEM) and a field-emission scanning electron microscope (SEM) equipped with an energy-dispersive X-ray spectrometer (EDX). For the TEM samples, the catalyst powder was dispersed in an alcohol solvent (Solmix AP-7, Japan Alcohol Trading Co., Ltd.) using ultrasonic waves for 5 min and a few drops of the suspension were cast onto carbon-coated copper grids (Cat. 653, Nisshin EM Co., Ltd.). The samples were dried overnight in the air at 80 °C. For SEM samples, a few drops of the same suspension were cast on an aluminum foil and dried overnight in the air at 80 °C. The TEM observations were performed using a JEM-2100 (JEOL Ltd.) at an accelerating voltage of 200 kV. SEM observations were performed using a JSM-7100F (JEOL Ltd.) at an accelerating voltage of 15 kV. The specific electrical resistances of the catalyst powders were measured using a powder resistivity measurement system (MCP-PD51, Nittoseiko Analytech Co. Ltd.). Approximately 15 mg of the catalyst powder was placed in a cylindrical holder and pressed at 60 MPa, after which the sample thickness and electrical resistance were measured. The specific electrical resistance is calculated by Eq. (2):

$$\rho = \frac{RA}{t} \tag{2}$$

where ρ, R, A, and t represent the specific electrical resistance (Ω cm), electrical resistance (Ω), sample cross sectional area (0.196 cm^2), and sample thickness (cm), respectively. The measurement results represent the specific electrical resistances of the catalyst nanoparticles and the carbon residue. The carbon residue in the sample was characterized using a microscopic Raman spectrometer (inVia Reflex, RENISHAW, λ = 532 nm). Approximately 10 mg of the catalyst powder was heated from room temperature to 1000 °C at a rate of 10 °C min^{-1} in air using a simultaneous thermogravimetric and differential thermal analyzer (DTG-60H, Shimadzu Corp.) to remove the carbon residue by combustion and evaluate the amount of carbon residue in the catalyst powder. The amount of carbon residue was determined by subtracting the weight of the residue from the initial weight. The Brunauer–Emmett–Teller (BET) specific surface area (S_{BET}) of the catalyst was evaluated using a surface area and pore size distribution analyzer (BELSORP Mini, MicrotracBEL Corp.) through N_2 gas adsorption. Prior to the measurement, the samples were heated at 120 °C under reduced pressure for 3 h to eliminate adsorbed moisture. The measurement results represent the specific surface areas of the catalyst nanoparticles and the carbon residue.

Electrochemical measurements

The electrochemical measurements were performed according to a previously reported procedures [10]. The sample (2.0 mg) was mixed with 1-hexanol (200 mm^3) and 1.0 wt.% Nafion® dispersion solution (10 mm^3) to prepare the catalyst ink. The 1.0 wt.% Nafion® dispersion solution was prepared by diluting a 5.0–5.4 wt.% Nafion® dispersion solution with a 1:1 mass ratio mixture of 1-propanol and ultrapure water. The catalyst ink was dropped on a polished glassy carbon rod (GC; $\varphi = 5.2$ mm, Tokai Carbon Co., Ltd.) and dried in air at 60 °C for 30 min to prepare the working electrode. The catalyst loading was approximately 0.5 $mg_{catalyst}$ cm^{-2}.

The measurements were performed in a static three-electrode cell with a potentiostat (SP-50, Bio-Logic Science Instruments) in 0.5 mol dm^{-3} H_2SO_4 (volumetric analysis grade, factor = 1.000, Fujifilm Wako Pure Chemical Corp.). A RHE and a GC plate were used as reference and counter electrodes, respectively. The cell temperature was maintained at 30 °C during the measurements. The electrode was cleaned by cycling between 0.05 and 1.1 V at a scan rate of 150 mV s^{-1} for 200 cycles in an O_2 atmosphere. Slow-scan voltammetry was performed under O_2 and N_2 atmospheres by sweeping from 0.2 to 1.1 V at a scan rate of 5 mV s^{-1}. The ORR current density (i_{ORR}) was obtained by subtracting the current density measured in the N_2 atmosphere from that measured in the O_2 atmosphere. Cyclic voltammetry (CV) was performed in an N_2 atmosphere, sweeping between 0.05 and 1.2 V at a scan rate of 50 mV s^{-1}. The electric double-layer capacitance (C_{dl}) was evaluated in the potential range of 0.8–1.0 V, where Faradaic peaks were not observed in the cyclic voltammograms and calculated using Eq. (3):

$$C_{dl} = \frac{i_{ave}}{v} \tag{3}$$

where C_{dl}, i_{ave}, and v represent the electric double-layer capacitance (F g^{-1}), average current in the anodic and cathodic directions at 0.8–1.0 V (A g^{-1}), and scan rate (mV s^{-1}), respectively. Furthermore, i_{ORR}, CV current, and C_{dl} were based on the mass of the catalyst powder (combined mass of the catalyst nanoparticles and carbon residue). The rest potential (E_{rest}) was measured by maintaining the electrode for 1 h under an O_2 atmosphere. In this study, E_{rest} was selected as an index to evaluate the activity of active sites. C_{dl} was selected as an index to evaluate the electron conduction path. Furthermore, i_{ORR} was selected as an index of the overall performance of the active sites and electron conduction path.

Results

Effect of gas atmosphere during heat treatment

Figures 2 and S1 show the XRD patterns of the samples heat-treated at 800 °C under the N_2 and NH_3 atmospheres. Both samples showed diffraction peaks corresponding to m-ZrO_2 (JCPDS File No. 37–1484) and t-ZrO_2 (JCPDS File No. 50–1089), with sharp diffraction peaks observed for the sample heat-treated in the NH_3 atmosphere. In addition, no diffraction peaks for oxynitrides or nitrides were observed for the NH_3 sample, and no shifts in the diffraction peaks of m-ZrO_2 or t-ZrO_2 were observed. The normalized Zr K-edge X-ray absorption near-edge structure (XANES) spectra are shown in Figure S2. The spectra of both samples closely resembled those of m-ZrO_2 or t-ZrO_2.

Table 1 lists the amount of carbon residue, S_{BET}, and the specific electrical resistance. The amounts of carbon residue were 23 and 68 wt.% for samples heat-treated in NH_3 and N_2 atmospheres, respectively, which indicates that heat treatment in an NH_3 atmosphere significantly decreased the amount of carbon residue. The S_{BET} was 110 and 43 m^2 g^{-1} for samples

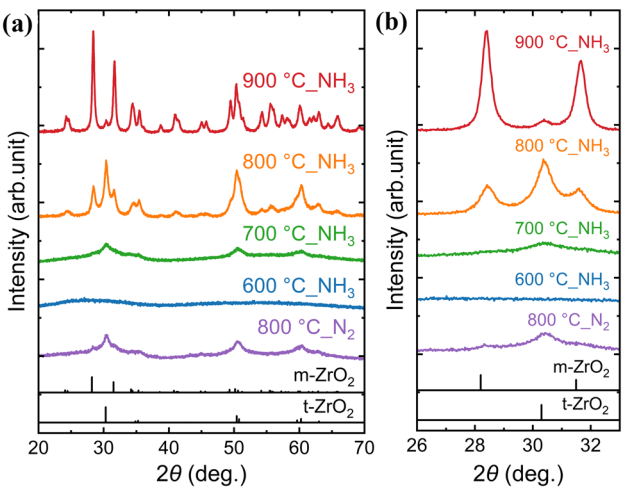

Figure 2 **a** XRD patterns and **b** enlarged view in the 26–33° region for the catalysts.

Table 1 Material properties and ORR activities for the catalysts

Sample	Crystallite size (nm)[1]		Chemical composition ratio (%)[2]		Amount of carbon residue (wt.%)[3]	S_{BET} ($m^2\ g^{-1}$)	Specific electrical resistance (Ω cm)[4]	C_{dl} ($F\ g^{-1}$)[5]	E_{rest} vs. RHE (V)[6]	i_{ORR} at 0.7 V (mA g^{-1})[7]
	m-ZrO_2	t-ZrO_2	m-ZrO_2	t-ZrO_2						
800°C_N_2	8.4	7.2	39	61	68	43	1.0	7.9	0.820	−4.4
600°C_NH_3	N/A	N/A	48	52	71	N/A	3.3×10^6	0.4	0.877	N/A
700°C_NH_3	3.0	5.5	39	61	46	242	3.3×10^6	0.9	0.882	N/A
800°C_NH_3	12.7	10.4	25	75	23	110	5.6×10^3	22.2	0.898	−113.2
900°C_NH_3	22.5	15.4	100	0	15	84	6.0×10^1	14.4	0.870	−55.2

[1]Crystallite size was calculated using Scherrer equation from the diffraction peaks of m-ZrO_2 ($\bar{1}$ 11) and t-ZrO_2 (101)

[2]Chemical composition ratio of the catalyst was estimated using LCF with reference spectra of m-ZrO_2 and t-ZrO_2

[3]Amount of carbon residue was calculated by heating the catalyst powder in the air and subtracting the residual weight from the initial weight

[4]Specific electrical resistance was measured under a pressure of 60 MPa applied to the catalyst powder

[5]C_{dl} was evaluated in the potential range of 0.8–1.0 V of the cyclic voltammogram

[6]E_{rest} was measured by maintaining the electrode for 1 h in an O_2 atmosphere

[7]i_{ORR} was obtained by subtracting the current density measured in an N_2 atmosphere from that in an O_2 atmosphere

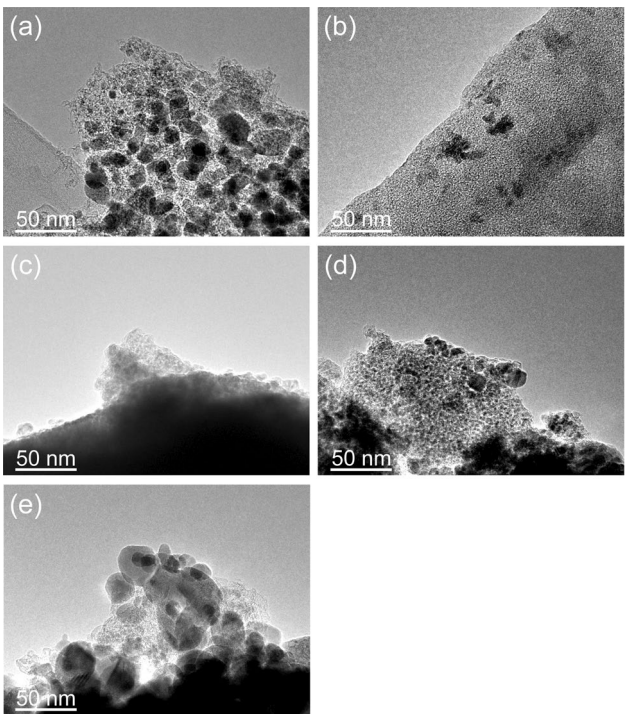

Figure 3 TEM images of **a** 800°C_N_2, **b** 600°C_NH_3, **c** 700°C_NH_3, **d** 800°C_NH_3, and **e** 900°C_NH_3.

heat-treated in NH_3 and N_2 atmospheres, respectively, with an increase in S_{BET} observed for the NH_3-treated sample. The specific electrical resistance was 5.6×10^3 and 1.0 Ω cm for samples heat-treated in NH_3 and N_2 atmospheres, respectively, and the specific electrical resistance increased by three orders of magnitude with heat treatment in an NH_3 atmosphere.

Figures 3 and S3 show the TEM images of both samples. In both samples, approximately 5 nm ZrO_2 nanoparticles were embedded in the carbon residue. In addition, approximately 20–30 nm ZrO_2 nanoparticles were observed. The amount of carbon residue decreased in the samples prepared in NH_3 atmosphere. Figures 4 and S4 show the SEM images. Several 10 μm powders were observed in both samples. Mesopores were observed on the surface of the carbon residue in the sample prepared in NH_3 atmosphere; whereas, macropores measuring several 100 nm were observed in the sample prepared in N_2 atmosphere.

Figure 5 and Table 1 present the cyclic voltammograms and C_{dl}. The CV current for the sample prepared in the NH_3 atmosphere was larger than that of the sample prepared in the N_2 atmosphere. In addition, the C_{dl} was 22.2 F g^{-1} and 7.9 F g^{-1} for samples heat-treated in NH_3 and N_2 atmospheres, respectively, indicating that heat treatment in an NH_3 atmosphere significantly increased C_{dl}.

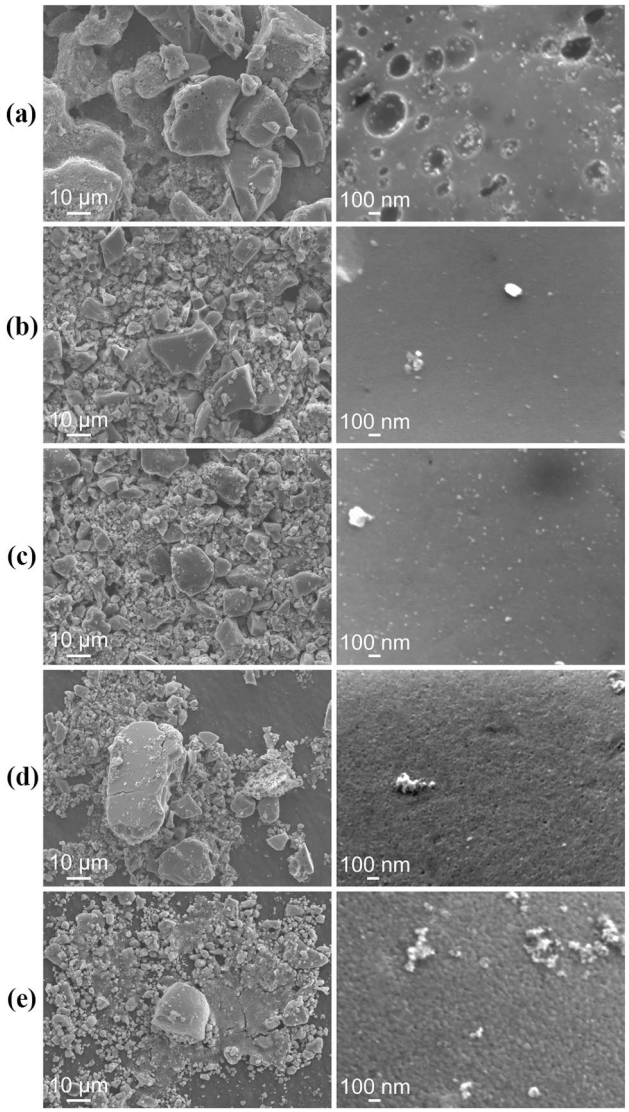

Figure 4 SEM images of **a** 800°C_N_2, **b** 600°C_NH_3, **c** 700°C_NH_3, **d** 800°C_NH_3, and **e** 900°C_NH_3. Low and high magnification images are shown on the left and right, respectively.

Effect of heat treatment temperature

Figures 2 and S1 show the XRD patterns of the samples heat-treated in an NH_3 atmosphere at temperatures ranging from 600 to 900 °C. The sample prepared at 600 °C did not exhibit any diffraction peaks; whereas, samples heat-treated at 700–900 °C displayed the diffraction peaks of m-ZrO_2 and t-ZrO_2. For the sample prepared at 900 °C, the intensity of the t-ZrO_2 diffraction peaks decreased, whereas that of m-ZrO_2 increased. In addition, no diffraction peaks of oxynitrides or nitrides and no shifts in the diffraction peaks

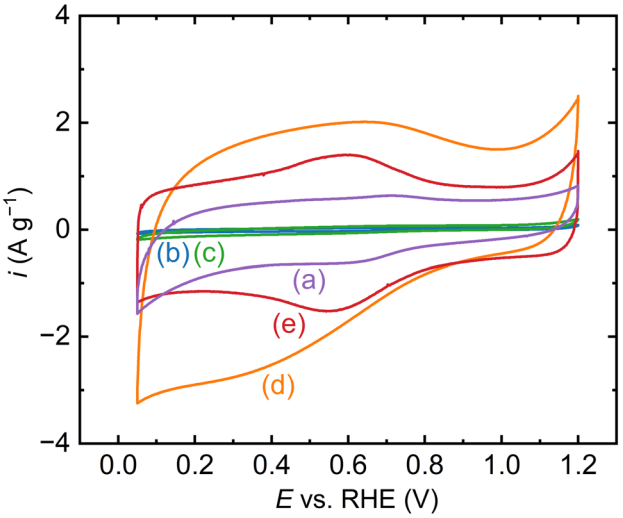

Figure 5 Cyclic voltammograms of a 800°C_N_2, b 600°C_NH_3, **c** 700°C_NH_3, **d** 800°C_NH_3, and **e** 900°C_NH_3.

of m-ZrO_2 or t-ZrO_2 were observed. The normalized Zr K-edge XANES spectra are shown in Figure S2. The spectra of each sample closely resembled those of m-ZrO_2 or t-ZrO_2.

Table 1 summarizes the amount of carbon residue, S_{BET}, and the specific electrical resistance. The amounts of carbon residue were 71, 46, 23, and 15 wt.% for samples heat-treated at 600, 700, 800, and 900 °C, respectively, indicating a reduction in the amount of carbon residue with increasing heat treatment temperature. The S_{BET} was 242, 110, and 84 $m^2\ g^{-1}$ for samples heat-treated at 700, 800, and 900 °C, respectively, and the S_{BET} decreased with an increase in the heat treatment temperature. The specific electrical resistance was 3.3×10^6, 3.3×10^6, 5.6×10^3, and 6.0×10^1 Ω cm for samples heat-treated at 600, 700, 800, and 900 °C, respectively, and it decreased by five orders of magnitude between 600 and 900 °C.

Figures 3 and S3 show the TEM images. ZrO_2 nanoparticles and carbon residues were observed in all samples. In the samples heat-treated at 600 and 700 °C, many ZrO_2 nanoparticles were embedded in the carbon residue. The amount of carbon residue decreased, exposing the ZrO_2 nanoparticles in the sample prepared at 800 °C. At 900 °C, the amount of carbon residue decreased further, and coarsening and agglomeration of the ZrO_2 nanoparticles were observed. Figures 4 and S4 show the SEM images of the samples. Several 10 μm powders were observed

in all samples. The carbon residue showed smooth surfaces in samples heat-treated at 600 and 700 °C. In contrast, mesopores were observed on the surface of the carbon residue in the sample prepared at 800 °C, which resulted in a rougher surface morphology. At 900 °C, the carbon residue covering the ZrO_2 nanoparticles decreased, forming aggregates of ZrO_2 nanoparticles.

Figure 5 and Table 1 present the cyclic voltammograms and C_{dl}. The CV current for samples heat-treated at 600 and 700 °C was very low. At 800 °C, the CV current increased sharply but then decreased at 900 °C. In addition, C_{dl} were 0.4, 0.9, 22.2, and 14.4 F g^{-1} for samples heat-treated at 600, 700, 800, and 900 °C, respectively, showing a sharp increase at 800 °C followed by a decrease at 900 °C.

Discussion

Effect of gas atmosphere on the material structure during heat treatment

The formation of zirconium oxide and carbon residues via the thermal decomposition of ZrPAA is also discussed. The bonds between the zirconium ions and polyacrylate dissociate when ZrPAA is heated to high temperatures. The dissociated polyacrylate undergoes thermal decomposition to produce carbon residues and various volatile decomposition products. McNeil et al. reported that the volatile decomposition products of polyacrylate include H_2O, CO_2, CO, and CH_4, among others [14]. Zirconium ions are oxidized by oxygen supplied by the polyacrylate to form zirconium oxide.

The XRD patterns displayed the diffraction peaks of m-ZrO_2 and t-ZrO_2 in the samples heat-treated in NH_3 and N_2 atmospheres. In addition, in the sample prepared in NH_3 atmosphere, the carbon residue covering the ZrO_2 nanoparticles decreased, promoting the grain growth of the ZrO_2 nanoparticles and resulting in sharp diffraction peaks for m-ZrO_2 and t-ZrO_2. However, diffraction peaks corresponding to oxynitrides or nitrides and peak shifts were not observed for the sample prepared in the NH_3 atmosphere. The XANES spectra confirmed that the chemical state of zirconium in both samples was a mixture of m-ZrO_2 and t-ZrO_2. The chemical composition ratio of the samples is listed in Table 1. The content of t-ZrO_2 increased in the sample prepared in the NH_3 atmosphere. Figure S5 shows the SEM–EDX spectra and elemental composition. Nitrogen was not detected in the sample prepared in the N_2 atmosphere but was present in trace amounts in the sample prepared in the NH_3 atmosphere, indicating that nitrogen may have been doped into either ZrO_2 or the carbon residue. However, neither the XRD patterns nor XANES spectra indicated the formation of zirconium oxynitrides or nitrides. Therefore, nitrogen doping is negligible in ZrO_2.

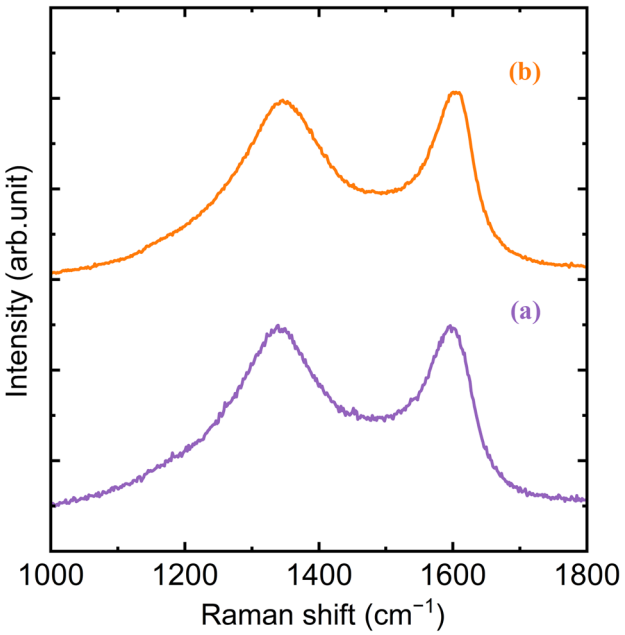

Figure 6 Raman spectra of the carbon residues for **a** 800°C_N_2 and **b** 800°C_NH_3.

Figure 6 shows the Raman spectra of the carbon residue. Not only the D-band around 1360 cm^{-1} associated with structural disorder but also the G-band around 1580–1600 cm^{-1} associated with the graphitic structure were observed in both samples. In addition, the R-values (I_D/I_G) obtained from the peak intensities of the D-band and G-band were 1.07 and 1.03 for samples heat-treated in NH_3 and N_2 atmospheres, indicating no significant difference in the R-value due to the gas atmosphere. Barbera et al. reported that graphitization of amorphous carbon occurs at heat treatment temperatures above 750 °C [15]. In the samples from this study, some carbon residue was graphitized, gaining conductivity and forming an electron conduction path connecting the active sites of the ZrO_2 nanoparticles to the current collector. S_{BET} increased despite a decrease in the amount of carbon residue

in the sample prepared in the NH_3 atmosphere. Van Dijen et al. reported that reactions occur when NH_3 decomposes into N_2 and H_2 at temperatures above 700 °C in an NH_3 atmosphere, and NH_3 reacts with C to produce HCN and H_2 [16].

$$2NH_3 \rightarrow N_2 + 3H_2 \quad (4)$$

$$C + NH_3 \rightarrow HCN + H_2 \quad (5)$$

A reduction in the amount of carbon residue in the sample heat-treated in the NH_3 atmosphere was assumed to result from the reaction described in Eq. (5). Katsura et al. investigated the reaction between non-graphitic carbon and NH_3 at 900 °C and reported that the main product of the carbon gasification reaction was CH_4 [17]. The possibility of CH_4 formation at 800 °C cannot be entirely excluded; however, it is considered negligible compared to the amount of HCN produced. In addition, the ZrO_2 nanoparticles covered by carbon residue were effectively exposed through gasification. In the SEM images, mesopores were observed on the surface of the carbon residue in the sample prepared in the NH_3 atmosphere. Chollon reported that carbon with a disordered structure was etched through the reaction described in Eq. (5) [18]. Therefore, it was inferred that the carbon residue was etched by NH_3 gas, leading to the formation of mesopores, which in turn contributed to the increase in S_{BET}. The specific electrical resistance of the sample prepared in the NH_3 atmosphere was three orders of magnitude higher than that of the sample prepared in the N_2 atmosphere. This is attributed to the lower amount of carbon residue in the sample heat-treated in NH_3 atmosphere (23 wt.%), which reflects the specific electrical resistance of the poorly conductive ZrO_2. Owing to the increase in S_{BET}, the sample heat-treated in an NH_3 atmosphere exhibited a larger C_{dl} than the sample heat-treated in an N_2 atmosphere. This suggests that the electrochemical effective surface area is greater, and the electron conduction path is improved. These results indicate that heat treatment in NH_3 atmosphere enhances the exposure of ZrO_2 nanoparticles and increases the specific surface area of the carbon residue, which is promising for the formation of an electron conduction path suitable for the ORR.

Effect of heat treatment temperature on the material structure

The XRD patterns indicated that an increase in the temperature from 600 to 800 °C improved the crystallinity of ZrO_2 nanoparticles, with t-ZrO_2 as the predominant phase. However, a phase transition from t-ZrO_2 to m-ZrO_2 occurred, and m-ZrO_2 became the dominant phase at 900 °C. The crystallite size of ZrO_2 nanoparticles increased with increasing heat treatment temperature. This result suggests that higher temperatures facilitate atomic diffusion or particle sintering, resulting in coarsening of ZrO_2 nanoparticles. Table 1 lists the chemical composition ratio of the samples obtained through the LCF analysis. The chemical state of zirconium was a mixture of m-ZrO_2 and t-ZrO_2 from 600 to 800 °C with the content of t-ZrO_2 increasing with an increase in heat treatment temperature. However, this trend changed, and at 900 °C, the chemical state transformed predominantly into m-ZrO_2. Although diffraction peaks corresponding to t-ZrO_2 were observed in the XRD pattern at 900 °C, their relatively low intensity suggests the minimal presence of t-ZrO_2. Therefore, t-ZrO_2 was not detected in the LCF semi-quantitative analysis owing to its small contribution to the XANES spectra. SEM–EDX analysis revealed trace amounts of nitrogen at 900 °C. Consequently, it is reasonable to conclude that, even at 900 °C, significant nitrogen doping of ZrO_2 by NH_3 gas was not observed. In the sample morphology, numerous ZrO_2 nanoparticles were covered by carbon residues at 600 and 700 °C, indicating that the number of effective active sites for ORR was limited. In contrast, ZrO_2 nanoparticles were exposed to 800 and 900 °C, indicating an increased number of effective active sites for the ORR.

The S_{BET} decreased with an increase in temperature from 700 to 900 °C. This reduction is caused by a decrease in the amount of carbon residue and/or the coarsening and aggregation of ZrO_2 nanoparticles. A considerable amount of carbon residue remained at 600 and 700 °C; however, the specific electrical resistance was high and C_{dl} was small. These results suggest that the amount of graphitized carbon residue in the samples was small and/or that graphitization was insufficient, resulting in an inadequate electron conduction path. At 800 °C, although the carbon residue decreased, the specific electrical resistance decreased by three orders of magnitude, indicating

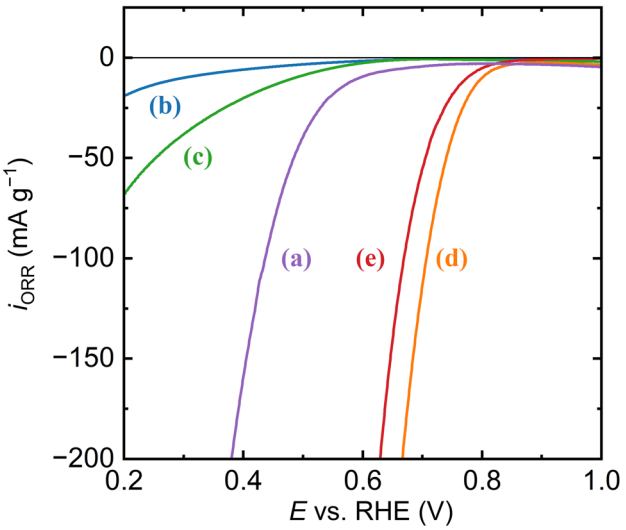

Figure 7 ORR polarization curves of **a** 800°C_N_2, **b** 600°C_NH_3, **c** 700°C_NH_3, **d** 800°C_NH_3, and **e** 900°C_NH_3.

that a portion of the carbon residue graphitized, enhancing conductivity. The large C_{dl} observed at 800 °C indicates an expanded electrochemical effective surface area, reflecting the formation of a sufficient electron conduction path. At 900 °C, the specific electrical resistance decreased further, enhancing the conductivity of the carbon residue. However, the decrease in C_{dl} implies a reduction in the electrochemical effective surface area, which is likely attributed to the decreased amount of carbon residue and suggests that some electron conduction path disappeared at 900 °C.

Effect of the material structure on the ORR activity

Figure 7 and Table 1 show the ORR polarization curves, E_{rest}, and i_{ORR} for the samples heat-treated under various gas atmospheres. The E_{rest} values of the samples heat-treated in N_2 and NH_3 atmospheres were 0.820 and 0.898 V vs. RHE, respectively, indicating a significant enhancement in E_{rest} caused by the heat treatment in NH_3 atmosphere. Moreover, the i_{ORR} of the samples prepared in the NH_3 atmosphere were several tens of orders of magnitude larger than those of the samples prepared in the N_2 atmosphere. This increase in i_{ORR} is likely attributed to the exposure of the ZrO_2 nanoparticles and the increased specific surface area of the carbon residue. These results indicate that heat treatment in an NH_3 atmosphere is promising for achieving a high E_{rest} and large i_{ORR}.

The E_{rest} values were 0.877, 0.882, 0.898, and 0.870 V vs. RHE at 600, 700, 800, and 900 °C, respectively, and E_{rest} improved between 600 and 800 °C. However, E_{rest} decreased at 900 °C. In addition, i_{ORR} was very low at 600 and 700 °C; however, it increased significantly at 800 °C. The i_{ORR} decreases at 900 °C. The reduction in E_{rest} and i_{ORR} at 900 °C is likely caused by a reduction in the electron conduction path caused by the loss of carbon residue. These results indicate that 800 °C is the optimal heat treatment temperature.

However, the ORR activity of the catalysts in this study was insufficient compared to that of state-of-the-art catalysts [12]. Consequently, future research should focus on a more detailed investigation of heat treatment conditions for the synthesis of highly active catalysts. In addition, a small amount of Fe was added to the catalyst precursor as a dopant to enhance ORR activity. It is possible that the Fe/N/C active sites were generated through heat treatment of the Fe-containing catalyst precursor in the NH_3 atmosphere and contributed to ORR activity. This aspect will be investigated in future studies.

Conclusion

A zirconium oxide-based catalyst for the ORR in PEFCs was synthesized via the heat treatment of ZrPAA in an NH_3 atmosphere. The structure of zirconium oxide, amount of carbon residue, conductivity, and morphology were precisely controlled by varying the gas atmosphere and temperature during the heat treatment. Heat treatment in an NH_3 atmosphere promoted the etching of the carbon residue, exposing the zirconium oxide nanoparticles and increasing the specific surface area of the carbon residue. At a heat treatment temperature of 800 °C, an optimal balance between the conductivity and amount of carbon residue was achieved, resulting in high E_{rest} and large i_{ORR}. This study demonstrated that heat treatment of ZrPAA in an NH_3 atmosphere effectively exposed zirconium oxide nanoparticles and enhanced the specific surface area of the carbon residue, providing valuable insights into the design of electron conduction paths suitable for the ORR. This method is expected to further enhance the ORR activity of metal oxide-based catalysts.

Acknowledgements

We appreciate the cooperation of Dr. Yuu Takeuchi (Institute of Advanced Sciences, Yokohama National University), Masayoshi Iwata and Kei Morimoto (School of Engineering, Osaka University) for their invaluable support during the experiments. This study was supported by the Japan Society for the Promotion of Science (JSPS) KAKENHI (Grant Nos. 23K04912 and 23KJ1509). The XAS experiments were performed at the NW10A beamline of KEK with the approval of the Photon Factory Program Advisory Committee (Proposal No. 2022G074).

Author contributions

Conceptualization contributed by Atsuhiro Ueno, Satoshi Seino, and Akimitsu Ishihara. Conducting experiments contributed by Atsuhiro Ueno, Yushi Tamaki, Yuta Uetake, Takaaki Nagai, and Ryuji Monden. Data analysis and investigation contributed by Atsuhiro Ueno. Writing—original draft preparation contributed by Atsuhiro Ueno and Satoshi Seino. Writing—review and editing contributed by Atsuhiro Ueno, Satoshi Seino, Yushi Tamaki, Yuta Uetake, Takaaki Nagai, Ryuji Monden, Akimitsu Ishihara, and Takashi Nakagawa. Funding acquisition contributed by Satoshi Seino and Yushi Tamaki. Resources contributed by Takashi Nakagawa and Akimitsu Ishihara. Supervision contributed by Satoshi Seino and Takashi Nakagawa.

Funding

Open Access funding provided by Osaka University. Funding was provided by Japan Society for the Promotion of Science, Grant No. 23K04912, Satoshi Seino, Grant No. 23KJ1509, Yushi Tamaki

Data and code availability

Not applicable.

Declarations

Conflicts of interest The authors declare that they have no competing interests.

Ethical approval Not applicable.

Supplementary Information The online version contains supplementary material available at https://doi.org/10.1007/s10853-025-10620-3.

References

[1] Bhoyate SD, Kim J, de Souza FM, Lin J, Lee E, Kumar A, Gupta RK (2023) Science and engineering for non-noble-metal-based electrocatalysts to boost their ORR performance: a critical review. Coord Chem Rev 474:214854. https://doi.org/10.1016/j.ccr.2022.214854

[2] Lian J, Zhao JY, Wang XM (2021) Recent progress in carbon-based materials of non-noble metal catalysts for ORR in acidic environment. Acta Metall Sin (Engl Lett) 34:885–899. https://doi.org/10.1007/s40195-021-01229-x

[3] Weiss J, Zhang H, Zelenay P (2020) Recent progress in the durability of Fe-N-C oxygen reduction electrocatalysts for polymer electrolyte fuel cells. J Electroanal Chem

875:114696. https://doi.org/10.1016/j.jelechem.2020.114696

[4] Seo J, Cha D, Takanabe K, Kubota J, Domen K (2013) Electrodeposited ultrafine NbO_x, ZrO_x, and TaO_x nanoparticles on carbon black supports for oxygen reduction electrocatalysts in acidic media. ACS Catal 3:2181–2189. https://doi.org/10.1021/cs400525u

[5] Ishihara A, Tamura M, Ohgi Y, Matsumoto M, Matsuzawa K, Mitsushima S, Imai H, Ota K (2013) Emergence of oxygen reduction activity in partially oxidized tantalum carbonitrides: roles of deposited carbon for oxygen-reduction-reaction-site creation and surface electron conduction. J Phys Chem C 117:18837–18844. https://doi.org/10.1021/jp405247m

[6] Okada Y, Ishihara A, Matsumoto M et al (2015) Effect of reheating treatment on oxygen-reduction activity and stability of zirconium oxide-based electrocatalysts prepared from oxy-zirconium phthalocyanine for polymer electrolyte fuel cells. J Electrochem Soc 162:F959. https://doi.org/10.1149/2.0201509jes

[7] Tominaka S, Ishihara A, Nagai T, Ota KI (2017) Noncrystalline titanium oxide catalysts for electrochemical oxygen reduction reactions. ACS Omega 2:5209–5214. https://doi.org/10.1021/acsomega.7b00811

[8] Chisaka M, Xiang R, Maruyama S, Daiguji H (2022) Twofold effects of zirconium doping into TiN on durability and oxygen reduction reactivity in an acidic environment. Energy Fuels 36:539–547. https://doi.org/10.1021/acs.energyfuels.1c03210

[9] Chisaka M, Shamim JA, Hsu WL, Daiguji H (2024) S-doped TiN supported N, P, S-tridoped TiO_2 with heterophase junctions for fuel cell startup/shutdown durability. J Mater Chem A 12:11277–11285. https://doi.org/10.1039/D4TA01475H

[10] Ishihara A, Nagai T, Ukita K et al (2019) Emergence of oxygen reduction activity in zirconium oxide-based compounds in acidic media: creation of active sites for the oxygen reduction reaction. J Phys Chem C 123:18150–18159. https://doi.org/10.1021/acs.jpcc.9b02393

[11] Shinyoshi N, Seino S, Uetake Y, Nagai T, Monden R, Ishihara A, Nakagawa T (2023) Radiation-induced synthesis of carbon-supported niobium oxide nanoparticle catalysts and investigation of heat treatment conditions to improve the oxygen reduction reaction activity. J Ceram Soc Jpn 131:575–580. https://doi.org/10.2109/jcersj2.23039

[12] Takeuchi Y, Watanabe K, Matsuzawa K, Nagai T, Ikegami K, Monden R, Ishihara A (2022) Enhancement of oxygen reduction activity of Fe-added zirconium oxide electrocatalysts without conductive supports in sulfuric acid. Chem Lett 51:927–931. https://doi.org/10.1246/cl.220283

[13] Tamaki Y, Seino S, Shinyoshi N et al (2024) Synthesis and characterization of titanium oxynitride catalyst via direct ammonia nitridation of titanium polyacrylate for oxygen reduction reaction. J Mater Sci: Mater Eng 19:40. https://doi.org/10.1186/s40712-024-00189-1

[14] McNeill IC, Sadeghi SMT (1990) Thermal stability and degradation mechanisms of poly (acrylic acid) and its salts: part 1-Poly (acrylic acid). Polym Degrad Stab 29:233–246. https://doi.org/10.1016/0141-3910(90)90034-5

[15] Barbera K, Frusteri L, Italiano G, Spadaro L, Frusteri F, Perathoner S, Centi G (2014) Low-temperature graphitization of amorphous carbon nanospheres. Chin J Catal 35:869–876. https://doi.org/10.1016/S1872-2067(14)60098-X

[16] Van Dijen FK, Pluijmakers J (1989) The removal of carbon or carbon residues from ceramic powders or greenware with ammonia. J Eur Ceram Soc 5:385–390. https://doi.org/10.1016/0955-2219(89)90043-5

[17] Katsura M, Nishimaki K, Nakagawa T, Yamamoto TA, Hirota M, Miyake M (1998) Thermodynamics of the formation of CH_4 by the reaction of carbon materials by a stream of NH_3. J Nucl Mater 258:839–842. https://doi.org/10.1016/S0022-3115(98)00119-6

[18] Chollon G (2021) The high temperature reaction of ammonia with carbon and SiC-C ceramics. J Eur Ceram Soc 41:136–147. https://doi.org/10.1016/j.jeurceramsoc.2020.08.066